A&A 464, 983–994 (2007)
DOI: 10.1051/0004-6361:20065653

Astronomy & Astrophysics

Probing the formation of intermediate- to high-mass stars in protoclusters

II. Comparison between millimeter interferometric observations of NGC 2264-C and SPH simulations of a collapsing clump

N. Peretto[1,4], P. Hennebelle[2], and P. André[1,3]

[1] Service d'Astrophysique, CEA/DSM/DAPNIA, C.E. Saclay, Orme des Merisiers, 91191 Gif-sur-Yvette, France
[2] Laboratoire de radioastronomie millimétrique, UMR 8112 du CNRS, École normale supérieure et Observatoire de Paris, 24 rue Lhomond, 75231 Paris Cedex 05, France
[3] AIM – Unité Mixte de Recherche CEA – CNRS – Université Paris VII – UMR 7158, France
[4] Department of Physics & Astronomy, University of Manchester, PO Box 88, Manchester M60 1QD, UK
e-mail: nicolas.peretto@manchester.ac.uk

Received 22 May 2006 / Accepted 30 October 2006

ABSTRACT

Aims. The earliest phases of massive star formation in clusters are still poorly understood. Here, we test the hypothesis for high-mass star formation proposed in our earlier paper (Peretto et al. 2006) stating that a massive, ultra-dense core may be currently forming at the center of the collapsing NGC 2264-C protocluster via the gravitational coalescence of several intermediate-mass Class 0 objects.
Methods. In order to confirm the physical validity of this hypothesis, we carried out IRAM Plateau de Bure interferometer observations of NGC 2264-C and performed SPH numerical simulations of the collapse of a Jeans-unstable, prolate dense clump. A detailed comparison between these hydrodynamic simulations and both our earlier IRAM 30 m observations and the new interferometer observations is presented.
Results. Our Plateau de Bure observations provide evidence for disk emission in three of the six Class 0-like objects identified earlier with the 30 m in the NGC 2264-C clump. Furthermore, they reveal the presence of a new compact source (C-MM13) located only ∼10 000 AU away, but separated by ∼1.1 km s^{-1} in (projected) velocity, from the most massive Class 0 object (C-MM3) lying at the very center of NGC 2264-C. Detailed comparison with our numerical SPH simulations supports the view that NGC 2264-C is an elongated cluster-forming clump in the process of collapsing and fragmenting along its long axis, leading to a strong dynamical interaction and possible protostar merger in the central region of the clump. The marked velocity difference observed between the two central objects C-MM3 and C-MM13, which can be reproduced in the simulations, is interpreted as an observational signature of this dynamical interaction. The present study also sets several quantitative constraints on the initial conditions of large-scale collapse in NGC 2264-C. Our hydrodynamic simulations indicate that the observed velocity pattern characterizes an early phase of protocluster collapse which survives for an only short period of time (i.e., $\leq 1 \times 10^5$ yr). To provide a good match to the observations the simulations require an initial ratio of turbulent to gravitational energy of only ∼5%, which strongly suggests that the NGC 2264-C clump is structured primarily by gravity rather than turbulence. The required "cold" initial conditions may result from rapid compression by an external trigger.
Conclusions. We speculate that NGC 2264-C is not an isolated case but may point to key features of the initial phases of high-mass star formation in protoclusters.

Key words. stars: formation – stars: circumstellar matter – stars: kinematics – ISM: clouds – ISM: kinematics and dynamics – hydrodynamics

1. Introduction

Most stars are believed to form in clusters (e.g. Lada & Lada 2003) and high-mass stars may form exclusively in cluster-forming clouds. For a comprehensive understanding of clustered star formation, a good knowledge of the initial conditions and earliest phases of the process is crucial which, in practice, can only be inferred from detailed studies of deeply embedded protoclusters at (sub)millimeter wavelengths (e.g. Motte et al. 1998; André 2002).

Two main scenarios have been proposed to explain the formation of high-mass stars in clusters. In the first scenario, high-mass stars form essentially in the same way as low-mass stars, via an enhanced accretion-ejection phase. In the standard model of low-mass star formation, the mass accretion rate is governed by the thermal sound speed and does not exceed $\sim 10^{-5}\ M_\odot\ \mathrm{yr}^{-1}$ (e.g. Shu 1977; Stahler et al. 2000) in cold cores. To form high-mass stars by accretion, a significantly higher accretion rate $\sim 10^{-3}\ M_\odot\ \mathrm{yr}^{-1}$ is required to overcome the radiation pressure generated by the luminous central object (e.g. Wolfire & Cassinelli 1987). In order to solve this problem, McKee & Tan (2003) proposed a model in which high-mass star formation takes place in ultra-dense cores supported by turbulence within virialized cluster-forming clumps. This model produces high-mass accretion rates such as those required to form high-mass stars by accretion.

In the second scenario, high-mass stars form by coalescence of lower-mass stars in the dense inner core of a contracting

protocluster (Bonnell et al. 1998). This scenario requires high stellar densities (i.e. $\sim 10^8$ stars pc^{-3}) in order to render the probability of stellar collisions high enough and allow stellar mergers to take place. It avoids the accretion problem of high-mass star formation by directly combining the masses of lower, intermediate-mass stars. However, no detailed model exists yet to describe how this coalescence mechanism actually occurs.

On the observational side, studying the earliest stages of high-mass star formation is particularly difficult due to the tight packing, deeply embedded nature, and relatively large distances of massive protoclusters. Based on IRAM 30 m observations of the massive cluster-forming clump NGC 2264-C ($d \sim 800$ pc), Peretto et al. (2006 – hereafter PAB06) recently proposed a picture of high-mass star formation combining features of the two above-mentioned scenarios. They showed that NGC 2264-C harbored a dozen Class 0-like objects (cf. André et al. 2000) and was characterized by large-scale collapse motions (see also Williams & Garland 2002). They suggested that a massive, ultra-dense protostellar core was in the making in the central part of the NGC 2264-C clump as a result of the gravitational merger of two or more lower-mass Class 0 objects. The total mass inflow rate associated with the collapse of the clump toward the central protostellar core was estimated to be $3\times10^{-3}\,M_\odot\,\mathrm{yr}^{-1}$. PAB06 argued that the combination of large-scale collapse and protostellar mergers may be the key to produce the conditions required for high-mass star formation in the center of NGC 2264-C.

In this paper, we follow up on the detailed single-dish study of NGC 2264-C by PAB06 and present higher-resolution observations of the same cluster-forming clump taken with the IRAM Plateau de Bure interferometer. We compare our observations with a set of SPH hydrodynamic numerical simulations which attempt to specifically model NGC 2264-C. As the kinematical and density patterns of NGC 2264-C appear to be relatively simple, comparison between millimeter observations of this region and numerical models offers a unique opportunity to make progress in our understanding of clustered star formation.

Section 2 presents our PdBI observations. Section 3 describes the dedicated hydrodynamic SPH simulations that we performed to model NGC 2264-C. We compare the observations with the numerical simulations in Sect. 4 and draw several conclusions in Sect. 5.

2. Interferometer observations of NGC 2264-C

2.1. Observations

We performed 3.2 mm and 1.2 mm observations of the central part of NGC 2264-C with the IRAM Plateau de Bure interferometer (PdBI) in December 2003 and April 2004. We used the C and D configurations with 6 antennas. We used both 1 mm and 3 mm receivers with 244.935620 GHz (λ = 1.2 mm) and 93.176258 GHz (λ = 3.2 mm) as central rest frequencies. We observed at four positions which were chosen so as to obtain a fully sampled mosaic at 3.2 mm (primary beam *FWHM* $\sim 54''$) and to encompass the millimeter sources C-MM1, C-MM2, C-MM3, C-MM4, CMM5, and C-MM9 (see Fig. 2b of PAB06) identified by PAB06 with the IRAM 30 m telescope. Because the corresponding 1.2 mm mosaic is undersampled (primary beam *FWHM* $\sim 20''$), only two of these sources (C-MM3 and C-MM4) were effectively imaged at 1.2 mm. We obtained a 3.2 mm dust continuum mosaic and two separate 1.2 mm continuum maps, as well as a $N_2H^+(1-0)$ mosaic. The spectral resolution for the $N_2H^+(1-0)$ data was 20 kHz, which corresponds to a velocity resolution of 0.06 km s^{-1} at 93.2 GHz. The sources used for the bandpass, amplitude and phase calibrations were 0420-014, 0528+134, 0736+017, CRL618, 0923+392, and 3C 273 (only the first three were used for the second run in April). We calibrated the data and produced images using the CLIC and MAPPING softwares (Lucas 1999; Guilloteau et al. 2002), part of the GILDAS package[1] (Pety 2005). The deconvolution was performed using the natural weighting option of the Clark (1980) CLEAN algorithm (Guilloteau 2001). The final synthesized beam was $5.3''\times3.8''$ (HPBW) with PA = +63° at 3.2 mm, and $3.1''\times1.5''$ (HPBW) with PA = +74° at 1.2 mm. We also combined our PdBI $N_2H^+(1-0)$ observations with the single-dish N_2H^+ data cube of PAB06 in order to recover short-spacing information. The resulting synthesized beam of the combined $N_2H^+(1-0)$ mosaic is $6.1''\times4.0''$ (HPBW) with PA = +65°.

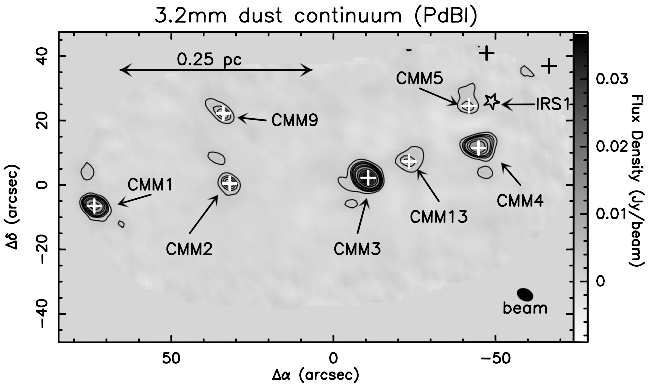

Fig. 1. 3.2 mm dust continuum mosaic of the central part of NGC 2264-C obtained with the PdBI. The (0″, 0″) position corresponds to (α = 06^{h}13^{m}00^s; δ = 09°29′10″) in J2000 coordinates. The pre/protostellar sources detected in this map are marked with white crosses and labelled C-MM, keeping the same numbering scheme as in PAB06. The two black crosses mark the positions of C-MM10 and C-MM12 (cf. PAB06), which are located at the very edge of our mosaic. The black open star shows the position of the luminous *IRAS* source IRS1. The rms of the mosaic is $\sigma \simeq 0.8$ mJy/beam. The contours are 2.4 mJy/beam (i.e. 3σ), 4 mJy/beam (i.e. 5σ), 5, 6, 8 mJy/beam and then go from 10 to 35 mJy/beam by 5 mJy/beam.

2.2. Dust continuum results: evidence for disk emission

Our PdBI 3.2 mm dust continuum mosaic is shown in Fig. 1. It reveals only pointlike sources, since most of the extended emission seen in the single-dish 1.2 mm dust continuum map (cf. Fig. 2 of PAB06) was filtered out by the interferometer. The final rms noise level was $\sigma \sim 0.8$ mJy/beam. We extracted millimeter sources from this map using the Gaussclump algorithm (Stutzki & Güsten 1990). We detected seven peaks lying above 5σ. All of these peaks were previously detected with the 30 m telescope, except one object, here called C-MM13 (cf. Fig. 1), which is a new detection. Several other peaks lie between 3σ and 5σ, but, by lack of confidence in these marginal detections, we did not consider them. The present 3.2 mm continuum map confirms and improves the positions of the compact millimeter continuum sources detected by PAB06. Interestingly our PdBI 1.2 mm continuum observations of C-MM3 and C-MM4 (not shown here) do not reveal any further sub-fragmentation. The source properties as derived from our PdBI and 30 m observations are summarized in Table 1.

[1] See `http://www.iram.fr/IRAMFR/GILDAS` for more information about the GILDAS softwares.

Table 1. Measured source properties.

Source	Coordinates (α_{2000} δ_{2000})	Undec. *FWHM*	PA	$S^{1.2}_{\rm peak}$	$S^{30\ {\rm m}}_{\rm peak}$	$S^{\rm exp:3.2}_{\rm peak}$	$S^{3.2}_{\rm peak}$	$S^{3.2}_{\rm int}$
		(arcsec)	(deg)	(mJy/beam)	(mJy/beam)	(mJy/beam)	(mJy/beam)	(mJy)
[1]	[2]	[3]	[4]	[5]	[6]	[7]	[8]	[9]
C-MM1	06:41:17.95 +09:29:03	5.8×4.1	63	–	255	6	18	21
C-MM2	06:41:15.15 +09:29:10	5.6×4.3	50	–	183	4	7	8
C-MM3	06:41:12.30 +09:29:12	5.7×4.4	58	224	573	14	37	45
C-MM4	06:41:09.95 +09:29:22	7.0×5.0	87	77	426	10	14	24
C-MM5	06:41:10.15 +09:29:36	6.2×4.5	83	–	261	6	5	7
C-MM9	06:41:15.30 +09:29:33	7.3×4.3	51	–	94	2	6	9
C-MM13	06:41:11.45 +09:29:17	7.5×6.1	87	–	–	–	5	11

[1]: The C-MM numbers are the same as in PAB06. The new source is labelled C-MM13. [2]: J2000 source coordinates, accurate to better than 1″, derived from a Gaussian fit to the PdBI 3.2 mm dust continuum map. [3]: Undeconvolved *FWHM* sizes derived from fitting an elliptical Gaussian to the PdBI 3.2 mm dust continuum map. [4]: Position angle (from North to East) of the major axis of the fitted Gaussian ellipse from the 3.2 mm dust continuum map. [5]: PdBI 1.2 mm peak flux density at the best-fit source position (HPBW = 3.1″ × 1.5″). [6]: 30 m 1.2 mm peak flux density at the source position (HPBW = 11″; from PAB06). [7]: 3.2 mm peak flux density expected at PdBI angular resolution estimated from Col. [6] (HPBW = 4.5″). [8]: PdBI 3.2 mm peak flux density at the best-fit source position (HPBW = 5.3″ × 3.8″). [9]: PdBI 3.2 mm integrated flux density inside the fitted Gaussian ellipse.

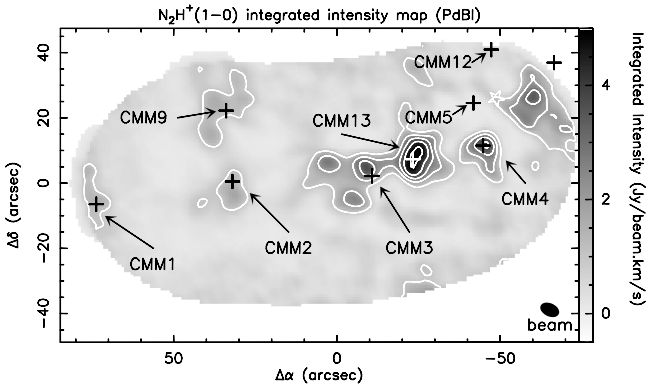

Fig. 2. $N_2H^+(1-0)$ integrated intensity map of the central part of NGC 2264-C obtained with the PdBI. The (0″, 0″) position corresponds to ($\alpha = 06^{\rm h}13^{\rm m}00^{\rm s}$; $\delta = 09°29'10''$) in J2000 coordinates. The crosses with labels show the positions of the pre/protostellar cores detected in our PdBI dust continuum mosaic (Fig. 1), while the black cross without label mark the position of C-MM10 (cf. PAB06). The white open star shows the position of the *IRAS* source IRS1. The contours go from 1 to 5 Jy beam^{-1} km s^{-1} by 1 Jy beam^{-1} km s^{-1}.

The millimeter dust continuum emission from a (Class 0 or Class I) protostar a priori originates from two components: an extended envelope (a few thousand AU in size) and a disk (up to a few hundred AU). At a distance of 800 pc, the linear resolution of the 30 m telescope is ∼9000 AU (HPBW) at $\lambda = 1.2$ mm. On this spatial scale, the 1.2 mm continuum emission observed toward a young protostar (Table 1 Col. [6]) is expected to be dominated by the envelope rather than by the disk (e.g. André et al. 2000; Looney et al. 2000). Conversely, we expect the disk component to dominate on compact, interferometric scales (e.g. Terebey et al. 1993). Assuming an isothermal, centrally-condensed envelope, i.e. with a density $\rho \propto r^{-2}$, the flux density is expected to scale linearly with beam size: $S_\nu \propto \theta$. We thus expect the envelope contribution to the PdBI flux density at 1.2 mm to be given by:

$$S^{\rm exp:1.2}_{\rm peak} = S^{30\ {\rm m}}_{\rm peak} \times \left(\frac{HPBW_{\rm Bure}}{HPBW_{30\ {\rm m}}} \right). \quad (1)$$

If we assume the Rayleigh-Jeans regime and adopt a dust opacity scaling as $\kappa_\nu \propto \nu^\beta$ (e.g. Hildebrand 1983), then we can also estimate the expected contribution of the envelope to the PdBI flux density at 3.2 mm:

$$S^{\rm exp:3.2}_{\rm peak} = S^{\rm exp:1.2}_{\rm peak} \times \left(\frac{1.2}{3.2} \right)^{\beta+2}. \quad (2)$$

In order to estimate a lower limit to the disk component, we choose $\beta = 1$ which maximizes the contribution of the envelope. A value of $\beta = 1.5$ is likely to be more representative of protostellar cores/envelopes (e.g. Ossenkopf & Henning 1994) and would yield a lower estimate for the expected envelope contribution. The expected envelope flux densities are listed in Table 1 Col. [7] for each detected source. It can be seen that they are a factor of ∼2−3 lower than the observed flux densities (Table 1 Col. [8]) for C-MM1, C-MM3 and C-MM9. The excess flux density observed on small spatial scales can be attributed to unresolved disk emission (e.g. Terebey et al. 1993). Our results thus suggest the presence of a disk in C-MM1, C-MM3, C-MM9 and confirm the protostellar nature of these candidate Class 0 sources. Given the uncertainties on the dust emissivity index β (e.g. Dent et al. 1998), we cannot conlude on the presence or absence of a disk in C-MM2 and C-MM4. Finally, it is very likely that C-MM5 does not have a disk since its observed 3.2 mm flux density is consistent with pure envelope emission.

For the three sources showing evidence of disk emission, i.e. C-MM1, C-MM3 and C-MM9, we can estimate both the disk and envelope masses as follows. First, we estimate the flux arising from the disk by subtracting the expected envelope peak flux density given in Table 1 Col. [7] from the observed peak flux density of Col. [8] (here, we assume that our 3.2 mm PdBI observations do not spatially resolve the disk given the distance of NGC 2264). Then, the flux arising from the envelope is considered to be given by the integrated flux of Col. [9] minus the disk contribution. These flux estimates are listed in Table 2. For the envelope mass estimates, we follow PAB06 and assume a dust temperature $T_{\rm d} = 15$ K, $\beta = 1.5$, as well as a dust opacity $\kappa_{1.2\ {\rm mm}} = 0.005$ cm^2 g^{-1} corresponding to $\kappa_{3.2\ {\rm mm}} = 1.3 \times 10^{-3}$ cm^2 g^{-1}. Concerning the disk mass estimates, we assume a dust temperature of $T_{\rm d} = 50$ K and a dust opacity $\kappa_{1.2\ {\rm mm}} = 0.02$ cm^2 g^{-1} (Beckwith et al. 1990) corresponding to $\kappa_{3.2\ {\rm mm}} = 5.2 \times 10^{-3}$ cm^2 g^{-1} (see Table 2). The dust temperature is higher for the disk because it is supposed to be warmer, closer to the star, while the dust opacity is slightly different from the one adopted in PAB06 because of the enhanced dust emissivity expected in the dense central parts of

Table 2. Estimated PdBI 3.2 mm flux densities of the disk and envelope components for the three objects showing evidence of disk emission.

Source	$S_{\rm disk}$ [a] (mJy)	$S^{\rm env}_{\rm peak}$ [b] (mJy/beam)	$S^{\rm env}_{\rm int}$ [c] (mJy)	$M_{\rm disk}$ [d] ($M_\odot$)
C-MM1	12	6	9	0.6
C-MM3	23	14	22	1.1
C-MM9	4	2	5	0.2

[a] 3.2 mm flux density of the disk component estimated by subtracting the peak flux density expected for the envelope (Col. [7] of Table 1) from the observed peak flux density (Col. [8] of Table 1). [b] Estimated 3.2 mm peak flux density of the envelope component at the PdBI resolution (cf. Col. [7] of Table 1). [c] 3.2 mm integrated flux density of the envelope component estimated by subtracting the disk contribution given in Col. [2] from the total integrated flux density measured with PdBI (cf. Col. [9] of Table 1). [d] Disk mass seen with the PdBI and estimated from $S_{\rm disk}$ (with $T_{\rm d}$ = 50 K and $\kappa = 5.2 \times 10^{-3}$ cm^2 g^{-1}). Typical uncertainty is a factor ≥2 (on either side) due to uncertain dust opacity and dust temperature.

protostellar disks (e.g. Ossenkopf & Henning 1994). We caution that the disk masses calculated in this way are only rough estimates. A more proper analysis of the density structure of these sources, especially C-MM3, through sub-arcsecond millimeter observations would be of great interest. By deconvolving the *FWHM* sizes of Table 1 from the synthesized beam, we derive the geometrical mean diameter of each source. For each object, we can then estimate the mean column density and mean volume density of the envelope component. All of these derived source parameters are listed in Table 3. It can be seen that C-MM3 and C-MM4 have the most massive envelopes by far, with $M_{\rm env} \geq 15\,M_\odot$ in both cases. The densest envelope/core is associated with the central source C-MM3, which reaches a mean volume density $\geq 1\times10^8$ cm^{-3} on a ∼3200 AU (2×*FWHM*) scale.

The new source identified with the interferometer, C-MM13, could not be separated from C-MM3 at the angular resolution of the IRAM 30 m telescope. The projected distance between C-MM3 and C-MM13 is only ∼10 000 AU. Surprisingly, C-MM13 is the only new compact millimeter continuum source detected with the PdBI above 5σ. The fact that there is almost no sub-fragmentation despite a factor 2−4 improvement in angular resolution between the partially resolved 30 m sources and their PdBI counterparts suggests that most of the compact dust continuum sources detected at the 30 m represent individual Class 0 objects rather than small groups of protostellar cores. However, we stress that our PdBI observations could only detect dust continuum sources with 3.2 mm peak flux densities larger than 4 mJy/beam (i.e. 5σ). Assuming the same temperature and dust properties as above for the envelope mass estimates, this corresponds to a mass detection threshold ∼3 $M_\odot$. Therefore, we could not have detected low-mass pre/protostellar cores possibly lying in the vicinity of the main sources listed in Table 1. This point is further discussed in the next section.

2.3. N_2H^+ (1–0) results

2.3.1. PdBI observations only

Our PdBI $N_2H^+(1-0)$ integrated intensity map is shown in Fig. 2. As for the dust continuum mosaic, most of the extended emission is filtered out. On this map, it can be seen that C-MM5 and possibly C-MM12 are not closely associated with a $N_2H^+(1-0)$ peak. We also note that the strongest $N_2H^+(1-0)$ peak is associated with the new C-MM13 object which is one of the weakest dust continuum sources. The morphological differences between the dust continuum sources and their $N_2H^+(1-0)$ counterparts may possibly reflect differences in chemical evolutionary stage (cf. Aikawa et al. 2005). It is also noteworthy that several $N_2H^+(1-0)$ peaks are not associated with any of the bona fide dust continuum sources listed in Table 3. On the other hand, most of these $N_2H^+(1-0)$ peaks have faint dust continuum counterparts with flux levels between 3σ and 5σ in the 3.2 mm continuum map (compare Figs. 1 and 2).

The $N_2H^+(1-0)$ spectra observed at PdBI (prior to combination with 30 m data) provide an estimate of the velocity dispersion within the sources on a ∼3500 AU (*FWHM*) spatial scale. The mean line-of-sight velocity dispersion is found to be $\langle\sigma_{\rm los}\rangle \simeq 0.34$ km s^{-1}. Assuming a kinetic temperature $T_{\rm k}$ = 15 K, the non-thermal contribution to this velocity dispersion is $\langle\sigma^{\rm NT}_{\rm los}\rangle \simeq 0.33$ km s^{-1}. Comparing this value with the isothermal sound speed, $c_s \simeq 0.23$ km s^{-1}, we conclude that the sources are still marginally dominated by non-thermal motions (due to, e.g., turbulence, collapse or, outflow) on scales of a few thousand AUs.

2.3.2. Combined PdBI and 30 m observations

As mentioned in Sect. 2.1, we added short-spacing 30 m information to our interferometric data in order to obtain a N_2H^+ map sensitive to a wide range of angular scales from ∼4″ up to ∼4′. This combination was performed using the MAPPING package developed by IRAM (Guilloteau et al. 2002). The combined PdBI/30 m map of $N_2H^+(1-0)$ integrated intensity is shown in Fig. 3. As expected, more extended emission is present in the combined mosaic, but the compact sources detected in the PdBI map are still clearly visible.

In order to constrain the kinematical pattern of these sources within the NGC 2264-C clump, we constructed a position-velocity (PV) diagram along an East-West axis going through the four central sources, C-MM2, C-MM3, CMM4, and C-MM13 (see Fig. 4). This PV diagram shows an overall velocity gradient of 8.4 km s^{-1} pc^{-1} from East to West between C-MM2 and C-MM4. The LSR velocities of each of the four sources C-MM2, C-MM3, C-MM4, and C-MM13 are listed in Table 3. Figure 4 helps to clarify the origin of the velocity discontinuity identified by PAB06 with the 30 m telescope in the center of NGC 2264-C (see Fig. 6 of PAB06). At the 30 m resolution, the $N_2H^+(101-012)$ spectrum observed toward the central source C-MM3 was double-peaked. The higher resolution of the PdBI interferometer now allows us to identify a distinct component, C-MM13, separated by 13″ in position and ∼1.1 km s^{-1} in velocity from C-MM3. With the 30 m telescope, C-MM13 could not be separated from C-MM3. We also observe in the western part of the PV diagram (at an offset of −70″ and velocity of 7.4 km s^{-1}) a velocity feature which is associated with the strong $N_2H^+(1-0)$ peak lying in this part of the clump (cf. Fig. 3). This velocity feature clearly departs from the rest of the diagram. We attribute it to a peculiar velocity field around the luminous young star IRS1, whose wind has likely perturbed the ambient velocity field and triggered star formation in the immediate vicinity (∼10″ in radius around IRS1), as suggested by the observations of Nakano et al. (2003) and Schreyer et al. (2003).

To summarize, our interferometric observations confirm the (Class 0) protostellar nature of C-MM1, C-MM3, C-MM9, and set new constraints on the kinematics of NGC 2264-C. The PdBI observations can help us to confirm or refute the scenario

Table 3. Derived source parameters.

Source	*FWHM*[a] (AU)	N_{H_2}[b] (10^{23} cm^{-2})	M_{env}[c] ($M_\odot$)	$M_{core}^{30\,m}$[d] ($M_\odot$)	n_{H_2}[e] (cm^{-3})	V_{LSR}[f] (km s^{-1})
C-MM1	1400	7	6.2	13.1	8.3×10^7	–
C-MM2	1400	9	5.5	16.0	7.3×10^7	6.2
C-MM3	1600	17	15.2	40.9	1.4×10^8	7.1
C-MM4	3000	17	16.5	35.1	2.2×10^7	8.9
C-MM5	2200	6	4.8	18.4	1.6×10^7	–
C-MM9	2400	2	3.5	6.6	9.3×10^6	–
C-MM13	4000	6	7.6	–	4.3×10^6	8.2

[a] Geometrical mean of the deconvolved, major and minor *FWHM* diameters measured on the PdBI 3.2 mm continuum mosaic. [b] Column density of the envelope seen with the PdBI and estimated from $S^{3.2}_{peak}$ for the sources without a disk (Col. [8] of Table 1) and from S^{env}_{peak} for the sources with a disk (Col. [3] of Table 2). The used dust properties are T_d = 15 K and $\kappa = 1.3\times10^{-3}$ cm^2 g^{-1}. Typical uncertainty is a factor ≥2 (on either side) due to uncertain dust opacity and dust temperature. [c] Envelope mass seen with the PdBI and estimated from S^{env}_{int} (Table 2; with T_d = 15 K and $\kappa = 1.3\times10^{-3}$ cm^2 g^{-1}). The uncertainty is the same as for the column density. [d] Core mass seen with the 30 m telescope (from PAB06). This mass is larger than M_{env} because, contrary to the PdBI, the 30 m does not filter out most of the large scale emission. [e] Envelope volume density estimated in a radius equal to the *FWHM*. Estimated in a radius twice smaller, the density increases by a factor of 4. The uncertainty is the same as for the column density. [f] LSR velocity estimated from the combined $N_2H^+(1-0)$ spectra.

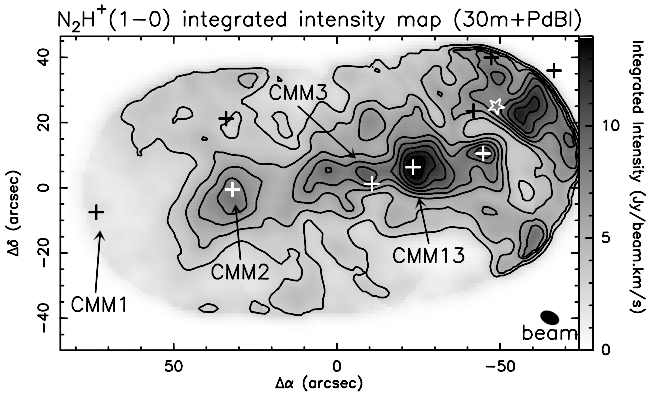

Fig. 3. $N_2H^+(1-0)$ integrated intensity map of the central part of NGC 2264-C resulting from the combination of our 30 m and PdBI data. The (0″, 0″) position corresponds to (α = 06^{h}13^{m}00^s; δ = 09°29′10″) in J2000 coordinates. The crosses mark the positions of the pre/protostellar 3.2 mm dust continuum sources detected in Fig. 1. For the sake of readability, only a few sources are labeled. The white open star symbol shows the position of the *IRAS* source IRS1. The contours go from 3 to 13 Jy beam^{-1} km s^{-1} by 2 Jy beam^{-1} km s^{-1}.

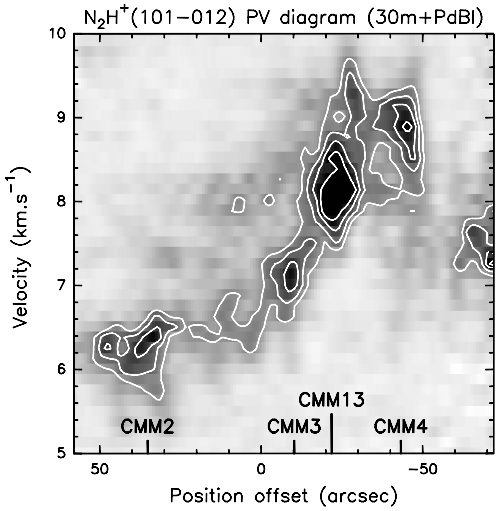

Fig. 4. Position-velocity diagram derived from the combined (PdBI + 30 m) N_2H^+(101-012) data cube by taking a cut along the East-West axis going through C-MM2, C-MM3, C-MM4 and C-MM13. The positions of these sources are plotted on the position axis. The white contours go from 0.5 to 1.1 Jy/beam by 0.2 Jy/beam.

proposed by PAB06 of an axial collapse of NGC 2264-C along its long axis leading to the merging of dense cores in the center. In the context of this scenario, the protostellar nature of the millimeter continuum cores sets strong timescale constraints: the individual collapse of the cores must occur on a significantly shorter timescale than the larger-scale collapse of the clump as a whole. The presence of two central sources, C-MM3 and C-MM13, adjacent to one another (i.e. 10 000 AU) and with a velocity difference of ∼1.1 km s^{-1}, must also be accounted for. In the next two sections, we attempt to match these observational constraints with hydrodynamic simulations.

3. SPH numerical simulations

3.1. Numerical method and initial conditions

In order to test the physical validity of the scenario proposed by PAB06 (see also Sect. 1), we performed Smooth Particle Hydrodynamics (SPH) simulations (Monaghan 1992; Bate et al. 2003) using the DRAGON SPH code from the Cardiff institute (see Goodwin et al. 2004). We simulated the time evolution of an isothermal (T_k = 20 K), Jeans-unstable elongated clump of mass 1000 $M_\odot$, comparable to the estimated total mass of NGC 2264-C (∼1600 $M_\odot$ – PAB06). The model clump was initially ellipsoidal (finite boundary conditions) with an aspect ratio of 2. The initial density profile was such as:

$$n_{H_2} = \frac{n_c}{(1 + (r/r_0)^2 + (z/2r_0)^2)} \quad (3)$$

corresponding to a flat inner ($r < r_0$) region and a $n_{H_2} \propto r^{-2}$ outer ($r > r_0$) region. The total mass of the flat inner region was ∼200 $M_\odot$. Highly concentrated clouds (with, e.g., $n_{H_2} \propto r^{-2}$) are known to hardly fragment during collapse (cf. Myhill & Kaula 1992; Whitworth et al. 1996), while uniform or moderately concentrated clouds (with $n_{H_2} \propto r^{-1}$ or flatter) typically fragment into as many Jeans-mass fragments as they contain initially (cf. Burkert et al. 1997). The expected number of fragments produced by the collapse of our model clump thus corresponds to the number of Jeans masses estimated in the flat inner core. At the mean density calculated within r_0

(i.e. $n_{H_2} \sim 1 \times 10^3$ cm^{-3}) and for $T_k = 20$ K, the Jeans mass is $M_J \simeq 20\ M_\odot$ (see Bonnell et al. 1996, for a precise definition of M_J), which yields a Jeans mass number $N_J \sim 10$ for the flat inner core. In these simulations we also included turbulent fluctuations. Since the exact nature and properties of interstellar turbulence are not fully understood yet, we considered two types of energy spectrum: 1) a spectrum scaling as Kolmogorov turbulence, i.e., $E(k) \propto k^{-5/3}$; and 2) a white spectrum, i.e., $E(k) \propto k^0$. The phases of these turbulence fluctuations were chosen randomly. Initially, three energy components controlled the evolution of the model filament: the thermal energy, $\mathcal{T}_{th}$, which remained constant in time throughout the simulations (i.e., isothermal assumption); the gravitational energy, $\mathcal{W}$, whose initial value depended on the clump density profile and thus on n_c and r_0 (larger values of n_c and/or r_0 correspond to lower gravitational energy; cf. Eq. (3)); and the turbulent energy, $\mathcal{T}_{turb}$. In all the simulations shown in this article, n_c and r_0 have the same value, namely $n_c(H_2) = 2000$ cm^{-3} and $r_0 = 0.7$ pc, corresponding to an initial thermal to gravitational energy ratio $\alpha^0_{th} \sim 8\%$. The initial value of the ratio of turbulent to gravitational energy, α^0_{turb}, was varied from 0% to 50%. We have also explored other initial conditions. When n_c is too large ($n_c > 5000$ cm^{-3}), we find that too many fragments form, when n_c is too small ($n_c < 500$ cm^{-3}), we find that only one central fragment will generally form. We have also varied the initial aspect ratio and conclude that if it is too close to one, then the cloud is not sufficiently filamentary whereas it is too much filamentary if it is initially too large. Finally, we have also explored the possibility that NGC 2264-C could be the result of a collision between two preexisting clouds rather than a collapsing elongated clump. However, it was not possible to reproduce the various features of this cloud within the scope of this scenario. The most important disagreements are i) a collision quickly tends to create a sheet rather than a filamentary object; ii) we find it very difficult to produce a well defined third object like C-MM3 by interaction of two colliding clouds; iii) a simple collision is unable to create a series of young condensations spread over the long axis of the clump at, e.g., positions comparable to C-MM1 and C-MM5. All our simulations were performed with a total of 5 million SPH particles. When the local density exceeded $n_{H_2} = 1.3 \times 10^8$ cm^{-3}, standard SPH particles were replaced by sink particles. The radius, $r_{sink} = 500$ AU, of the sink particles defines the highest resolution reached by our simulation. All particles falling within r_{sink} of a sink particle and being bound to it were removed from the simulations, and their mass, linear and angular momentum were added to the corresponding sink particle values. Using sink particles allowed us to avoid artificial fragmentation (Truelove et al. 1997; Bate & Burkert 1997). The relatively low density threshold at which sink particles were introduced implies that we could not model advanced phases of star/cluster formation but only the first stages of clump fragmentation. Indeed, the limited numerical resolution of our simulations prevented us from describing small spatial scale processes such as disk formation.

3.2. General pattern

Figure 5 displays the density and velocity fields along the z-axis (i.e., long axis), as well as the column density maps in the (z, x) plane, at four time steps for a model filament with an initial level of turbulence, $\alpha^0_{turb} = 5\%$. The reference time was chosen to be at one global free-fall time, t_{ff}, after the start of the simulation. Given the initial central density of the model clump, this corresponds to $t_{ff} = 9.5 \times 10^5$ yr. The four time steps shown in Fig. 5 were taken at $t_{ff} - 4\times10^5$ yr, $t_{ff} - 2\times10^5$ yr, $t_{ff} - 1.0\times10^5$ yr, and $t_{ff} - 0.4 \times 10^5$ yr, respectively.

We can describe the evolution of the model clump as follows (see also Bonnell et al. 1996; Inutsuka & Miyama 1997). Since the ellipsoidal clump initially contains several thermal Jeans masses (i.e. $N_J \sim 10$, cf. Sect. 3.1) and has a shorter dynamical timescale perpendicular to its major axis, it first collapses along its minor axis when seen projected onto the plane of the sky (see first and second panels of Fig. 5), amplifying the initial anisotropy and leading to the formation of a very elongated and filamentary structure (cf. Lin et al. 1965). This fast contraction proceeds until thermal and turbulent pressure gradients can stop the collapse along the minor axis, ensuring an approximate hydrostatic equilibrium in the (xy) plane (cf. Bonnell et al. 1996).

Since the dynamical timescale is longer along the major axis, the clump keeps collapsing along its long axis, i.e. the z-direction, after a transverse equilibrium has been established. The velocity field is initially nearly homologous (i.e., $V_z \propto z$ – see first and second panels of Fig. 5) but becomes more and more complex as the filament fragments into several cores, each of them collapsing individually as can be seen on the third and fourth panels of Fig. 5. The individual collapse of the cores leads to the formation of local protostellar accretion shocks and associated protostars. Moreover, due to the global collapse of the model clump toward its center, we can also see the formation of a central shock which separates the eastern ($z > 0$) and western ($z < 0$) sides of the clump. Altogether this dynamical evolution produces a complex density and velocity pattern.

When $\alpha^0_{turb} = 50\%$, the velocity field (not displayed here for conciseness) is much less organized. More shocks develop which lead to enhanced clump fragmentation through the process now widely referred to as "turbulent fragmentation" in the literature (e.g. Padoan & Nordlund 2002; Klessen et al. 2005). The number of shocks is larger and the model clump becomes more substructured as the initial level of turbulence increases (see also Jappsen & Klessen 2004). At the other extreme, the case with no initial turbulence at all, $\alpha^0_{turb} = 0\%$, does not yield any fragmentation due to the lack of initial fragmentation seeds, which is not realistic.

Therefore, based on the results of our simulations, several general conclusions can be drawn. In particular, the initial level of turbulence appears to play a key role for the global aspect of the model clump. The higher the turbulence, the more dispersed and less filamentary the model clump is. For low levels of initial turbulence, i.e., low values of α^0_{turb}, the structure and kinematics of the clump are dominated by gravity, while for high levels of turbulence the clump is primarily structured by turbulence.

4. Detailed comparison between the observations and the SPH simulations

We performed a wide set of SPH simulations with different initial parameters, e.g., different values of the initial level of turbulence, α^0_{turb}, and of the thermal to gravitational energy ratio, α^0_{th}. We did not find it necessary to use different initial turbulent velocity fields since the time evolution of the model clump depends only weakly on this. When calculating synthetic observations, we varied the inclination angle of the long axis of the model clump with respect to the line of sight. An inclination angle of 45 degrees was adopted to produce the synthetic images and diagrams shown in Figs. 6 and 7. For each set of simulations, we seeked a particular time step at which the synthetic data, when convolved to the resolution of the observations,

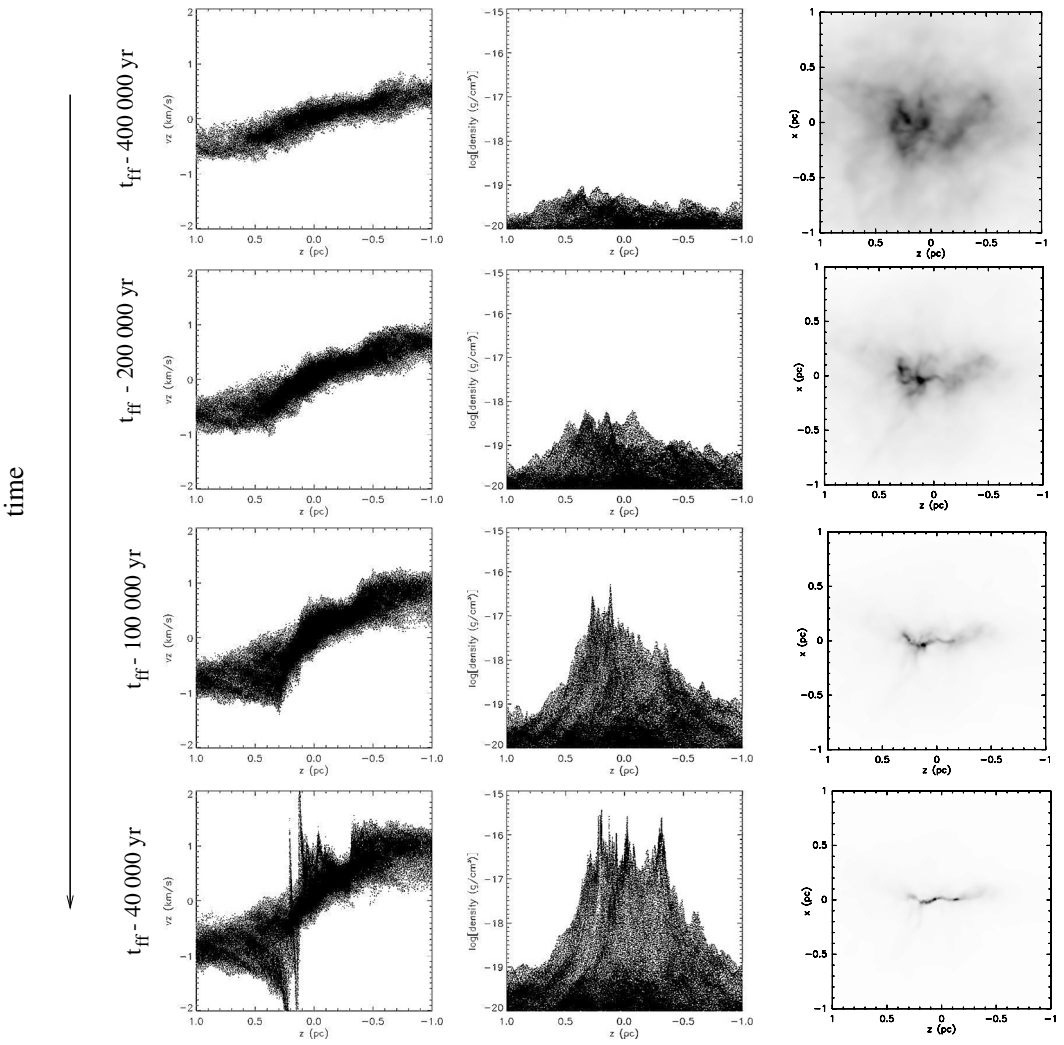

Fig. 5. Time evolution of a simulation with an initial turbulent to gravitational energy ratio $\alpha^0_{\rm turb}$ = 5%. The first column displays the velocity field of the particles taken along the long axis (z-axis) of the model filament, as traced by individual SPH particles. The second column similarly displays the evolution of the density cut along the z-axis of the model filament. The third column shows synthetic column density maps in the (z, x) plane. The reference time, labelled $t_{\rm ff}$, is taken to be one global free-fall time of the initial clump after the start of the simulation, i.e., $t_{\rm ff} = 9.5 \times 10^5$ yr. The first row is taken at a time step $t_{\rm ff} - 4 \times 10^5$ yr, while the second, third, and fourth rows are for time steps $t_{\rm ff} - 2 \times 10^5$ yr, $t_{\rm ff} - 1.0 \times 10^5$ yr, and $t_{\rm ff} - 0.4 \times 10^5$ yr, respectively.

best matched the existing 30 m and PdBI constraints. In the next subsection, we present our "best-fit" simulations and discuss the consequences of changing the best-fit parameters.

4.1. Overall morphology: a fragmented filament

The first important feature which must be reproduced by the simulations is the elongated shape of NGC 2264-C and the presence of several protostellar sources, lining up along the long (East-West) axis of the clump.

Figure 6 compares the observed column density maps (first row) with synthetic maps obtained from simulations with four different initial levels of turbulence, i.e., $\alpha^0_{\rm turb}$ = 1% (second row), $\alpha^0_{\rm turb}$ = 5% (third row), $\alpha^0_{\rm turb}$ = 20% (fourth row), and $\alpha^0_{\rm turb}$ = 50% (fifth row), all assumed to be "observed" with a viewing angle of 45 degrees. The first column of Fig. 6 displays the synthetic data convolved to the 30 m resolution while the second column displays the data convolved with the PdB interferometer beam. When convolving the simulated data to the PdBI resolution, we included the effect of interferometric filtering so as to allow more direct comparison with the observations. For this purpose, we used the UV_MODEL task of the GILDAS package. This task generated a set of visibilities in the UV plane by calculating the values of the Fourier transform of the simulated input image at the observed UV baselines. The rest of the points in the UV plane was set to zero. This method had the consequence of filtering out all extended structures present in the numerical simulations.

The four simulations shown in Fig. 6 are compared when the synthetic column density maps convolved to the 30 m resolution match the observed map best, except for the case with $\alpha^0_{\rm turb}$ = 50% (cf. fifth row) which does not exhibit a filamentary shape at any time step in the simulation. The corresponding time steps all lie in the range between $t_{\rm ff} - 5 \times 10^5$ yr and $t_{\rm ff} - 1.5 \times 10^5$ yr. The total mass accreted onto sink particles at these time steps ranges from 0% to 0.2% of the initial clump mass. As already mentioned, we are thus looking at the very first stages of the formation of a protocluster, i.e., when the first pre-/proto-stellar cores with typical mean volume densities $\sim 10^5$ cm^{-3} appear. It can also be seen in Fig. 6 that the filamentary, elongated appearance of the NGC 2264-C clump

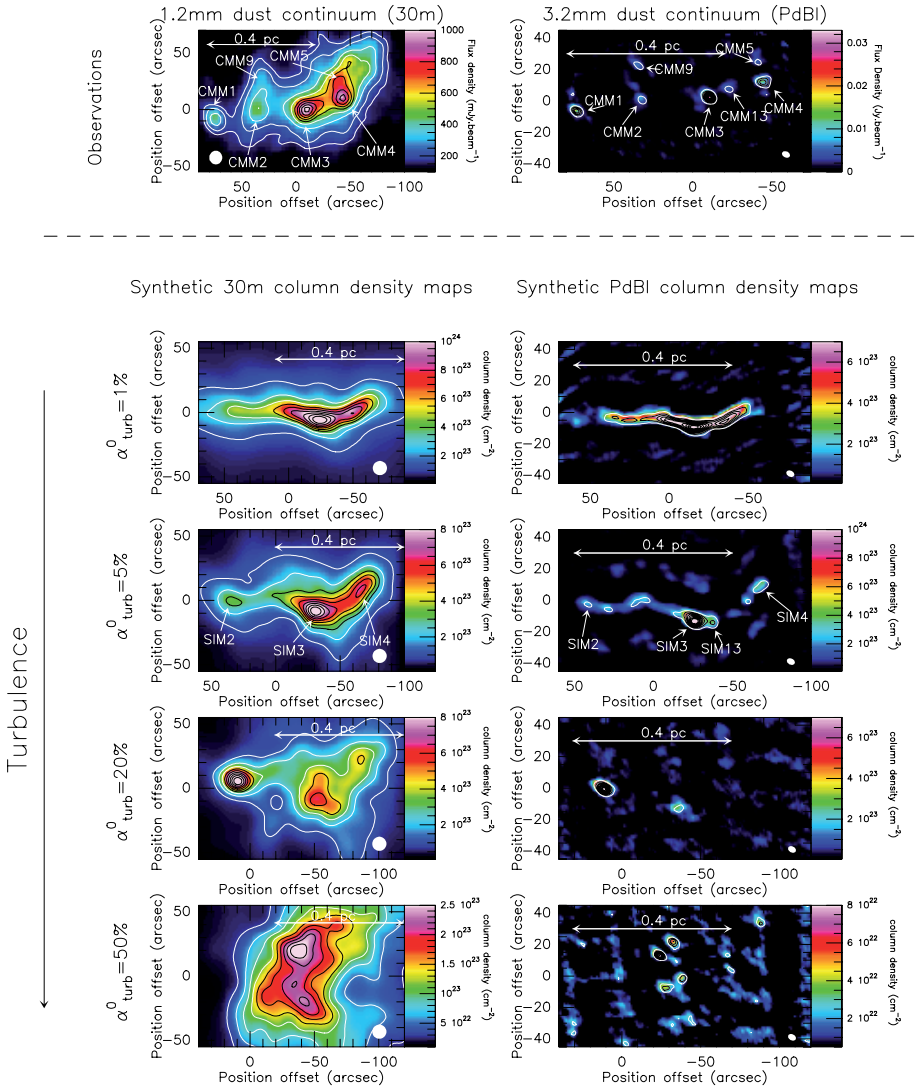

Fig. 6. Observed column density distribution (*first row*) compared to synthetic column density maps (*second to fifth row*) convolved to the 30 m angular resolution (*first column*) and to the PdBI angular resolution (*second column*) for four different initial levels of turbulence: $\alpha^0_{\rm turb}$ = 1% (*second row*), $\alpha^0_{\rm turb}$ = 5% (*third row*), $\alpha^0_{\rm turb}$ = 20% (*fourth row*), $\alpha^0_{\rm turb}$ = 50% (*fifth row*). The best-fit simulation corresponds to the third row, i.e., $\alpha^0_{\rm turb}$ = 5% (for which the displayed time step is the "best-fit" time step). Note that the synthetic PdBI maps include the effect of interferometric filtering (see text). In each map, the contour levels go from 10 to 90% by step of 10% of the peak emission. The observed 30 m column density distribution corresponds to the 1.2 mm dust continuum map of PAB06.

cannot be reproduced when the initial level of turbulence is too high in the model. Based on this argument, we conclude that $\alpha^0_{\rm turb}$ has a maximum value of 20%, although the 5% model already provides a better match to the observations than the 20% model. Figure 6 also shows that the large-scale morphology of the clump observed at the resolution of the 30 m telescope provides the strongest discriminator between different values of $\alpha^0_{\rm turb}$.

Our "best-fit" simulation is shown in the third row of Fig. 6. It corresponds to a flat energy spectrum, $E(k) \propto k^0$, and an initial value of $\alpha^0_{\rm turb}$ = 5%, which is much lower compared to other numerical SPH studies of cloud fragmentation (e.g. Bate et al. 2003). Note that the case of Kolmogorov-like turbulence leads to results which are broadly similar to that shown in Fig. 6, except that the shape of the filament is more irregular and too distorted to match the observations well. We therefore restrict our attention to the $E(k) \propto k^0$ case. Although this energy spectrum differs from the classical Kolmogorov one, we argue in Sect. 5 that it is not unrealistic on the parsec scale of the NGC 2264-C clump.

Comparison between the observed dust continuum maps of NGC 2264-C and the synthetic column density maps of the "best-fit" simulation (see Fig. 6) shows that the number of fragments and their alignment are well reproduced. By analogy with the observations, we have labelled the three main fragments of the synthetic 30 m column density map SIM2, SIM3 and SIM4. The corresponding synthetic PdBI map shows a strong central source, SIM3, surrounded by weaker sources, as observed. Moreover an additional component, labelled SIM13, becomes visible next to SIM3 in the simulations when "observed" at the PdBI angular resolution, which is strongly reminiscent of the (C-MM3, C-MM13) system in the real interferometric map.

As described in Sect. 3.2, the collapse of the filament proceeds in two main phases: first, a global contraction velocity field is established along the long axis; second, a strong shock is generated at the center by the two interacting sides of the model clump. At the same time, the clump fragments to form protostars. Thus, there are at least two relevant dynamical timescales in the problem: a global dynamical timescale corresponding to the global evolution of the elongated clump, and a local dynamical timescale corresponding to the dynamical evolution of individual fragments. In other words, there is competition between local collapse (i.e. fragmentation) and global collapse. In our simulations, this is controlled by the ratio of thermal to gravitational energy, $\alpha^0_{\rm th}$, and thus by $n_{\rm c}$ and r_0 (whose values are 2000 cm^{-3} and 0.7 pc, respectively) since the kinetic temperature and the mass of the model clump are fixed (cf. Sect. 3.1). If $n_{\rm c}$ or r_0 are too small (i.e. the density structure approaches $n_{\rm H_2} \propto r^{-2}$; cf. Eq. (3)), the individual fragments do not have enough time to collapse on their own before entering the

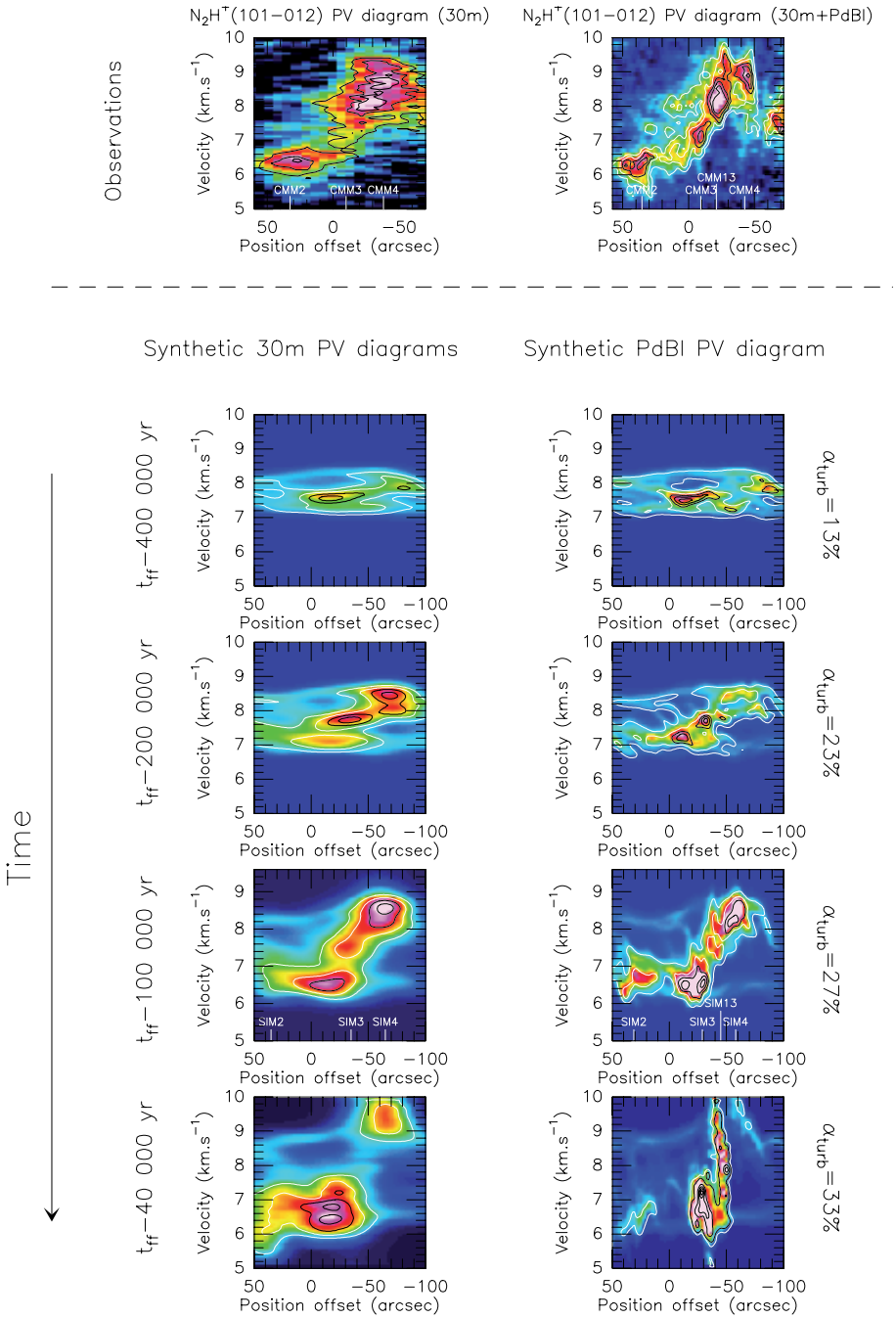

Fig. 7. Observed position-velocity diagrams (*first row*) compared to synthetic position-velocity diagrams (*second to fifth row*) convolved to the 30 m angular resolution (*first column*) and to the PdBI angular resolution (*second column*) at four different time steps of our best-fit SPH simulation ($\alpha^0_{\rm turb}$ = 5%): $t_{\rm ff}-400\,000$ yr (*second row*); $t_{\rm ff}-200\,000$ yr (*third row*); $t_{\rm ff}-100\,000$ yr (*fourth row*); $t_{\rm ff}-40\,000$ yr (*fifth row*) (with $t_{\rm ff} = 9.5 \times 10^5$ yr). The best-fit time step corresponds to fourth row. The value of the turbulent to gravitational energy ratio $\alpha_{\rm turb}$ at each time step is given on the right hand side. Note that $\alpha_{\rm turb}$ increases as time proceeds in the simulation.

central shock. Therefore only one, massive central core forms. Conversely, if $n_{\rm c}$ and r_0 are too large, many protostars (and eventually stars) form before any significant large-scale velocity field is established along the clump long axis. Furthermore, in the latter case, the number of fragments produced in the simulations becomes larger than the observed number of fragments.

Note that the collapse simulations shown in this paper were performed with model clumps of total mass $M_{\rm tot} = 1000\,M_\odot$, while the total mass of NGC 2264-C is estimated to be somewhat larger, ∼1600 $M_\odot$ (cf. PAB06). With more massive model clumps, we did not manage to reproduce the overall morphology of NGC 2264-C, in the sense that too much fragmentation occurred. This suggests that our models lack some source of support against gravity compared to the actual NGC 2264-C clump. This will be discuss further in Sect. 5.

4.2. The sharp central velocity discontinuity

One of the most interesting features of NGC 2264-C is the central velocity discontinuity observed by PAB06 in optically thin tracers toward C-MM3 (see Fig. 7). This velocity discontinuity is believed to trace the axial (i.e., 1D) collapse of NGC 2264-C along its long axis, as well as a possible dynamical interaction between protostellar sources at the center of the clump. Our new PdBI observations, which confirm the presence of a strong velocity gradient along the long axis of the clump (i.e. ∼8.4 km s^{-1} pc^{-1} – see Fig. 4), set additional constraints on the velocity field in the central part of NGC 2264-C.

When the initial level of turbulence was lower than 20%, our SPH simulations convolved to the 30 m resolution led to a central discontinuity resembling that observed. Furthermore, the shape of the PV diagram observed at the PdBI resolution along

the long axis of the clump appears to be a key tracer of the time evolution, as can be seen in Fig. 7. In addition to observed PV diagrams (first row), Fig. 7 shows the synthetic PV diagrams of our "best-fit" simulation ($\alpha^0_{\rm turb} = 5\%$) convolved to the 30 m resolution (first column) and to the PdBI resolution (second column) at the same four time steps as in Fig. 5 (rows two to five). Note that simulations adopting a Kolmogorov-like turbulent energy spectrum and low values of $\alpha^0_{\rm turb}$ ($\leq$20%) led to velocity discontinuities which are similar to the discontinuity shown here for the "best-fit" simulation.

The reference time in Fig. 7 is the same as in Fig. 5, namely one global free-fall time ($t_{\rm ff} = 9.5 \times 10^5$ yr) after the start of simulation. At the first time step shown, $t_{\rm ff} - 4 \times 10^5$ yr (second row), no clear kinematical signature is apparent in the synthetic PV diagrams, either at the 30 m or at the PdBI resolution. At $t_{\rm ff} - 2 \times 10^5$ yr (third row), the synthetic PV diagrams start to exhibit a velocity structure reminiscent of the observed velocity gradient and central discontinuity, but the amplitude of the velocity structure is not large enough to match the observations. At the best-fit time step, i.e., $t_{\rm ff} - 1 \times 10^5$ yr, the agreement between the simulated PV diagrams (fourth row) and the observed PV diagrams (first row) is quite remarkable. The central amplitude (i.e. $\sim$2 km s^{-1}), shape, and position of the velocity discontinuity are well reproduced. Moreover, the synthetic PdBI PV diagram shows a $\sim$1 km s^{-1} velocity gap between the two central fragments, SIM3 and SIM13, as observed between C-MM3 and C-MM13.

The fifth row of Fig. 7 shows a later time, i.e., $t_{\rm ff} - 0.4 \times 10^5$ yr, when the central shock is well developed. While the synthetic 30 m PV diagram remains satisfactory, the synthetic PdBI PV diagram differs markedly from the observations. Note, however, that this late phase of evolution may not be correctly described by our numerical model. Indeed, our simulations do not include feedback from protostars which clearly influences the late dynamical evolution of cluster-forming clouds (cf. Li & Nakamura 2006). Thus, it is not clear if, in reality, the central shock would have time to develop as much as in the simulations to produce a PV diagram such as the one shown at the bottom right of Fig. 7.

The time evolution of the $\alpha_{\rm turb}$ ratio in the "best-fit" simulation is also given on the right-hand side of Fig. 7. While the initial level of turbulence was only $\alpha^0_{\rm turb} = 5\%$ in this simulation, it can be seen the ratio of nonthermal kinetic energy to gravitational energy quickly increases up to $\alpha_{\rm turb} = 27\%$ at the "best-fit" time step and $\alpha_{\rm turb} = 33\%$ at the last time step shown. This demonstrates that the bulk of the "turbulent" energy in our simulations does not come from the large scale turbulent velocity field, but rather from the conversion of gravitational energy into kinetic energy through the global collapse of the clump. The increase of $\alpha_{\rm turb}$ with time contributes to produce synthetic linewidths in reasonable agreement with observed linewidths (see Sect. 4.3 and Fig. 8 below), despite the low level of kinetic energy at the beginning of the simulation. We also note that the value of $\alpha_{\rm turb}$ achieved at the "best-fit" time step (27%) is within a factor of 2 of the kinetic to gravitational energy ratio expected in virial equilibrium (50%), despite the fact that the model clump is globally collapsing and far from equilibrium at this stage. Clearly, the broad linewidths observed in NGC 2264-C result at least partly from systematic inward motions as opposed to random turbulence. In our "best-fit" model, most of the motions are gravitationally focussed and do not exert any support against gravitational collapse.

4.3. Large-scale kinematical pattern in optically-thin line tracers

The $H^{13}CO^+(1-0)$ spectra observed toward NGC 2264-C with the 30 m telescope show a remarkable East-West axial symmetry over the whole clump on either side of the central source C-MM3 (see Fig. 8). The low optical depth of the $H^{13}CO^+(1-0)$ line ($\tau \sim 0.3$ for the peak velocity channel of the central spectrum) inferred from the Monte-Carlo radiative transfer calculations of PAB06 implies that the observed double-peaked line profiles (cf. Fig. 8) result from the presence of two velocity components along the line of sight rather than from self-absorption. Although our PdBI observations show that the central velocity discontinuity seen with the 30 m telescope originates from two unresolved protostellar sources, the large spatial extent of the region over which double-peaked $H^{13}CO^+(1-0)$ spectra are observed in the 30 m map suggests a global kinematical origin for the double-peak profiles.

While the $N_2H^+(101-012)$ PV diagram observed with PdBI (Fig. 4) may be suggestive of rotation about an axis perpendicular to the long axis of the clump, PAB06 showed that rotation could not account for the shape of the observed 30 m PV diagram based on a detailed comparison with radiative transfer models (see Fig. 12 of PAB06). By contrast, we now proceed to show that our scenario of large-scale, axial collapse does provides a good match to the symmetric pattern of double-peaked line profiles observed in low optical depth tracers.

To this aim, synthetic spectra were constructed from our SPH simulations assuming strictly optically thin line tracers: each SPH particle was given the same weight and the contributions of all particles falling within a given velocity channel were integrated. The synthetic data cube was then convolved to the 30 m angular resolution and normalized in such a way that the peak intensity of the synthetic central spectrum matched the peak intensity of the observed central $H^{13}CO^+(1-0)$ spectrum. Figure 8 compares the $H^{13}CO^+(1-0)$ spectra observed in the central part of NGC 2264-C (top) with the resulting synthetic spectra for the best-fit simulation at the best-fit time step (bottom). (In this comparison, we use the observed $H^{13}CO^+(1-0)$ spectra rather than the observed $N_2H^+(1-0)$ spectra since the former have a better signal-to-noise ratio.) It can be seen that the overall agreement is very good. Since the synthetic line emission is optically thin, the double-peaked spectra exhibited by the model are clearly not due to radiative transfer effects but result from the presence of two velocity components along the line of sight, corresponding to the two ends of the elongated clump moving toward each other. Focusing on the central row of spectra (marked in boldface), it can be seen that the blue-shifted component of the double-peaked spectra dominates on the eastern side. Moving west, the red-shifted component becomes progressively stronger. It is nearly as intense as the blue-shifted component at the central position and eventually dominates on the western side of the filament. This remarkable reversal of blue/red spectral asymmetry as one moves from the eastern to the western side of the central C-MM3 position can be seen in both the observations and simulations.

The synthetic spectra obtained from our SPH simulations are mass weighted and are thus more representative of the global kinematics of the clump than of the kinematics of compact individual fragments. We conclude that the remarkable pattern seen in the central row of spectra in Fig. 8 characterizes the collapse of the elongated clump along its long axis. We note, however, that the synthetic spectra are somewhat narrower than are the observed $H^{13}CO^+(1-0)$ spectra. Part of the observed linewidths

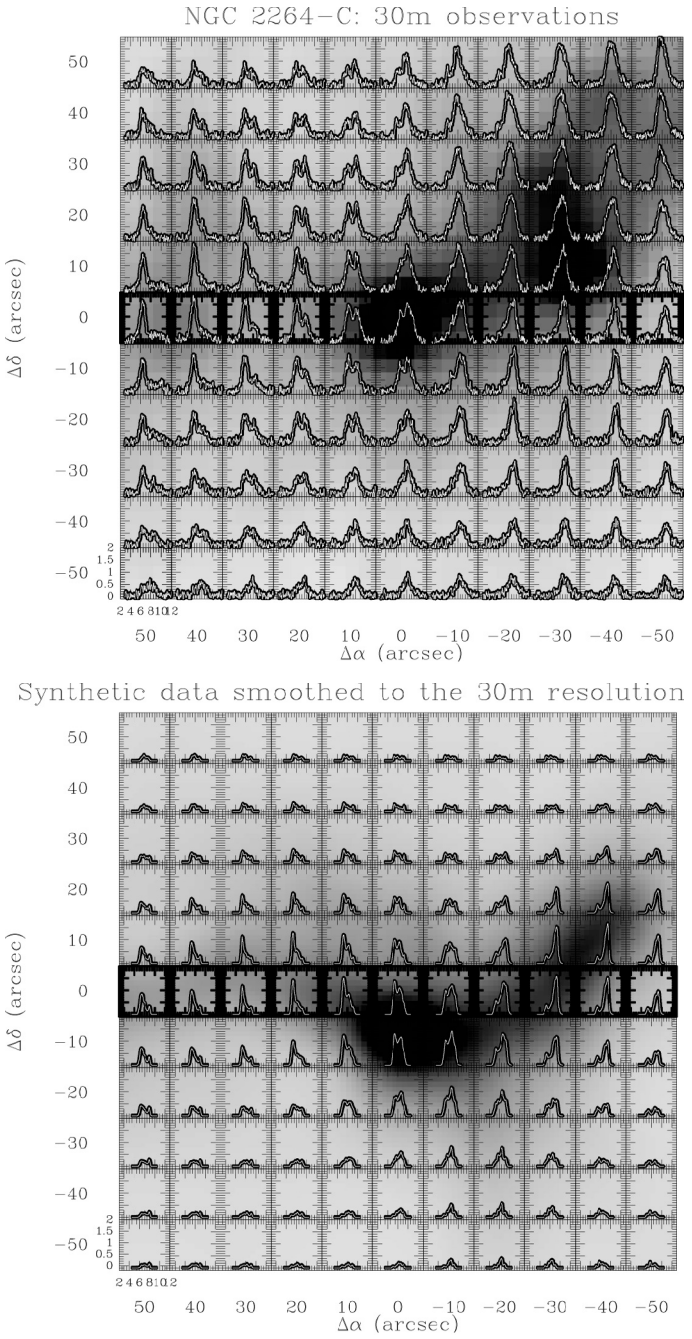

Fig. 8. Comparison between the $H^{13}CO^+(1-0)$ spectra observed at the 30 m telescope (*upper panel*) and the synthetic optically thin spectra obtained in our best-fit simulation (*lower panel*). In the *upper panel*, the (0, 0) corresponds to the position of C-MM3, while in the *lower panel* the (0, −10) position corresponds to the position of SIM3. Overlaid in grey scale are the 1.2 mm dust continuum image of PAB06 (*top*) and the synthetic column density map of the best-fit simulation (*bottom*). The row of spectra observed (*top*) and simulated (*bottom*) along the main axis of the clump are marked in boldface.

may result from outflowing gas generated by the protostars, an effect which we did not treat in our simulations. It may also be partly due to another source of support against gravity, not included in our simulations (see Sect. 5).

In the context of our interpretation of the double-peaked spectral pattern observed in $H^{13}CO^+(1-0)$, the extent of the region over which the red-shifted peak is observed on the eastern side (and the blue-shifted peak observed on the western side) sets constraints on the diameter of the NGC 2264-C cylinder-like clump (see Fig. 11 of PAB06). Double-peaked $H^{13}CO^+(1-0)$ spectra are observed up to 30″ on either side of the central object C-MM3. Given the distance of 800 pc and assuming a viewing angle of 45 degrees between the line of sight and the long axis of the clump (as adopted in the radiative transfer model presented by PAB06), we estimate the diameter of the cylinder to be ∼0.65 pc. This is in good agreement with the apparent width of the NGC 2264-C clump as measured in the plane of sky on our dust continuum and molecular line maps.

5. Concluding remarks

The good quantitative agreement obtained between our "best-fit" SPH simulations and our (30 m and PdBI) millimeter observations confirms the physical plausibility of the scenario of large-scale axial collapse and fragmentation proposed by PAB06 for the NGC 2264-C clump. Observationally, such an axial collapse is traced by a central velocity discontinuity associated with double-peaked profiles in optically thin line tracers. The present study supports our earlier suggestion that an ultra-dense protostellar core of mass up to $\sim 90\,M_\odot$ is in the process of forming at the center of NGC 2264-C through the dynamical merging of lower-mass Class 0 cores (cf. PAB06). Our interferometric PdB detection of a new object, C-MM13, located only ∼10 000 AU away (in projection) from the central source, C-MM3, but with a line-of-sight velocity differing by ~ 1.1 km s^{-1} from that of C-MM3, provides an additional observational manifestation of the merging process. Given the relatively large mass of C-MM13 ($\sim 8\,M_\odot$), such a large velocity difference would be difficult to explain by dynamical fragmentation during the collapse of an individual protostellar core, even if low-mass objects can easily be ejected from dynamically unstable protostellar systems (e.g. Bate et al. 2003; Goodwin et al. 2004). In our proposed scenario for NGC 2264-C, the local collapse of individual protostellar cores is strongly influenced by the high dynamical pressure resulting from the global collapse of the clump, and proceeds in a manner that is qualitatively similar to the triggered protostellar collapse models discussed by Hennebelle et al. (2003, 2004).

Our detailed comparison between observations and simulations has also allowed us to set constraints on the evolutionary state of the NGC 2264-C protocluster. It seems that the characteristic shape of the observed position-velocity diagrams survives for a relatively short period of time, i.e. $\leq 1\times10^5$ yr, and occurs only very soon after the formation of the protocluser while less than ∼1% of the gas has been accreted onto sink particles.

The low level of initial turbulent energy required to match the observations implies that NGC 2264-C is structured more by self-gravity than by turbulence. The main effect of turbulence is to create seeds for further gravitational fragmentation. Turbulent fragmentation does not appear to play a significant role in this clump. In our "best-fit" simulation, the initial turbulent to gravitational energy ratio is $\alpha^0_{\rm turb} = 5\%$, comparable to the ratio of thermal to gravitational energy $\alpha^0_{\rm th}$. The level of "turbulence" increases as the simulation proceeds and gravitational energy is converted into kinetic energy. At the "best-fit" time step, the ratio of nonthermal kinetic energy to gravitational energy approaches ∼30%. Most of the corresponding "turbulence" is gravitationally generated as in the recent cloud collapse simulations of Burkert & Hartmann (2006). In other words, the cloud motions in our best-fit model are primarily due to collapse and gravitationally organized motions as opposed to purely random turbulence. Although we have not identified a specific trigger,

we believe that the "cold" or "subvirial" initial conditions (cf. Adams et al. 2006) required by our model reflect the fact that the NGC 2264-C clump was suddenly compressed and/or assembled as a result of a strong external perturbation.

The fact that simulations starting from initial turbulent velocity fields with a Kolmogorov-like energy spectrum lead to model clumps that are much less organized than the observations should not be overinterpreted. Indeed, since the phases are chosen randomly and since in Kolmogorov-like turbulence most of the energy is on large scales, it is not surprising that the shape of the filament is strongly distorted in this case. In a real situation, the large-scale turbulent fluctuations should be much more coherent since they may be responsible, at least in part, for the formation of the filament in the first place (cf. Hartmann et al. 2001).

Another point worth noting is that the total mass of gas with density above 10^4 cm^{-3} is $\sim$10 times lower in our best-fit simulation than in the actual NGC 2264-C clump. Using higher densities by a factor of 10 in the numerical simulations would inevitably lead to fragmentation into a larger number of cores since the corresponding Jeans mass would be smaller by a factor $\sim$3 compared to the Jeans mass in the present simulations. It seems therefore that some additional support against gravity, not included in the simulations presented here, plays a role in NGC 2264-C. This extra support could arise from protostellar feedback and/or magnetic fields.

Finally, we speculate that the evolution inferred and simulated here for NGC 2264-C is not exceptional but representative of many massive cluster-forming clumps in the Galaxy. In particular, we note that evidence of large-scale, supersonic inward motions has been recently found in several deeply embedded regions of high-mass star formation (Motte et al. 2005; see also Wu & Evans 2003; and Fuller et al. 2005). NGC 2264-C may just be caught at a particularly early stage of protocluster evolution and observed in a favorable configuration, leading to a remarkably simple kinematical pattern. Similar detailed modelling studies of other cluster-forming clumps will be needed to confirm this hypothesis.

Acknowledgements. We are grateful to the IRAM astronomers in Grenoble for their help with the Plateau de Bure interferometric observations. IRAM is supported by INSU/CNRS (France), MPG (Germany), and IGN (Spain).

References

Adams, F. C., Proszkow, E. M., Fatuzzo, M., & Myers, P. C. 2006, ApJ, 641, 504
Aikawa, Y., Herbst, E., Roberts, H., & Caselli, P. 2005, ApJ, 620, 330
André, P. 2002, Ap&SS, 281, 51
André, P., Ward-Thompson, D., & Barsony, M. 2000, in Protostars and Planets IV, ed. V. Mannings, A. Boss, & S. Russell (Tucson: Univ. Arizona Press), 59
Bate, M., & Burkert, A. 1997, MNRAS, 288, 1060
Bate, M., Bonnell, I., & Bromm, V. 2003, MNRAS, 339, 577
Beckwith, S., Sargent, A., Chini, R., & Güsten, R. 1990, AJ, 99, 924
Bonnell, I., Bate, M., & Price, N. 1996, MNRAS, 279, 121
Bonnell, I., Bate, M., & Zinnecker, H. 1998, MNRAS, 298, 93
Burkert, A., & Hartmann, L. 2006, ApJ, 616, 288
Burkert, A., Bate, M., & Bodenheimer, P. 1997, MNRAS, 289, 497
Dent, W., Matthews, H., & Ward-Thompson, D. 1998, MNRAS, 301, 1049
Di Francesco, J., André, P., & Myers, P. 2004, ApJ, 617, 425
Fuller, G. A., Williams, S. J., & Sridharan, T. K. 2005, A&A, 442, 949
Goodwin, S., Whitworth, A., & Ward-Thompson, D. 2004, A&A, 423, 169
Guilloteau, S. 2001, in Proceedings from the IRAM Millimeter Summer School 2, ed. A. Dutrey, 219
Guilloteau, S., Lucas, R., & Bouyoucef, K. 2002, Mapping cookbook IRAM Plateau de Bure Interferometer, Version 1.3 (IRAM)
Hartmann, L., Ballesteros-Paredes, J., & Bergin, E. 2001, ApJ, 562, 852
Hennebelle, P., Whitworth, A., Gladwin, P., & André, P. 2003, MNRAS, 340, 870
Hennebelle, P., Whitworth, A., Cha, S.-H., & Goodwin, S. 2004, MNRAS, 348, 687
Hildebrand, R. 1983, QJRAS, 24, 267
Inutsuka, S.-I., & Miyama, S. 1997, ApJ, 480, 681
Jappsen, A.-K., & Klessen, R. A&A, 423, 1
Lada, C., & Lada, E. 2003, ARA&A, 41, 57
Li, Z. Y., & Nakamura, F. 2006, ApJ, 640, L187
Lin, C. C., Mestel, L., & Shu, F. H. 1965, ApJ, 142, 1431
Looney, L., Mundy, L., & Welch, W. 2000, ApJ, 529, 477
Lucas, R. 1999, CLIC manual, version 4.1 (IRAM)
Mc Kee, C., & Tan, J. 2003, ApJ, 585, 850
Monaghan, J. 1992, ARA&A, 30, 543
Motte, F., André, P., & Neri, R. 1998, A&A, 365, 440
Motte, F., Bontemps, S., Schilke, P., et al. 2005, in Massive star birth: a crossroads of astrophysics, ed. R. Cesaroni et al. (Cambridge University Press), IAU Symp. 227, 151
Myhill, E., & Kaula, W. 1992, ApJ, 386, 578
Nakano, M., Sugitani, K., & Morita, K. 2003, PASJ, 55, 1
Ossenkopf, V., & Henning, T. 1994, A&A, 291, 943
Padoan, P., & Nordlund, A. 2002, ApJ, 576, 870
Peretto, N., André, P., & Belloche, A. 2006, A&A, 445, 979 (PAB06)
Pety, J. 2005, SF2A-2005: Semaine de l'Astrophysique Française, ed. F. Casoli, T. Contini, J.-M. Hameury, & L. Pagani (Les Ulis: EDP Sciences), 721
Schreyer, K., Stecklum, B., Linz, H., & Henning, T. 2003, ApJ, 599, 335
Stahler, S., Palla, F., & Ho, P. 2000, in Protostars and Planets IV, ed. V. Mannings, A. Boss, & S. Russell (Tucson: Univ. Arizona Press), 327
Shu, F. 1977, ApJ, 214, 488
Stutzki, J., & Güsten, R. 1990, ApJ, 356, 513
Terebey, S., Chandler, C., & André, P. 1993, ApJ, 414, 759
Truelove, J., Klein, R., McKee, C., et al. 1997, ApJ, 489, 179
Whitworth, A., Bhattal, A., Francis, N., & Watkins, S. 1996, MNRAS, 283, 1061
Williams, J., & Garland, C. 2002, ApJ, 568, 259
Wolfire, M., & Cassinelli, J. 1987, ApJ, 319, 850
Wu, J., & Evans, N. J. II 2003, ApJ, 592, L79